Formation and Characterisation of Polymetallic Rings in vacuo

Niklas Geue[1,*], Grigore A. Timco[2], George F. S. Whitehead[2], Eric J. L. McInnes[2], Neil A. Burton[2], Richard E. P. Winpenny[2] and Perdita E. Barran[1,*]

[1]Michael Barber Centre for Collaborative Mass Spectrometry, Manchester Institute of Biotechnology, Department of Chemistry, The University of Manchester, 131 Princess Street, Manchester, M1 7DN, UK. [2]Department of Chemistry, The University of Manchester, Oxford Road, Manchester, M13 9PL, UK.

[*]Corresponding Authors: niklas.geue@manchester.ac.uk, perdita.barran@manchester.ac.uk

Abstract

Understanding the (dis)assembly mechanisms of large metallosupramolecules is critical in their design, stability and diverse applications. Yet this task is difficult because of the inherent complexity of the structures, with many potential pathways of combining (or separating) the constituent building blocks. Here, we use collision-induced dissociation mass spectrometry to study the disassembly of heterometallic complexes, which have attracted interest due to their potential properties as new materials. Collisional activation leads to the formation of a series of previously unknown smaller ring products and we characterise their geometry using ion mobility. Specifically, the disassembly of both {$\mathbf{Cr_xCu_2}$} hourglass structures (x = 10, 12) and of a {$\mathbf{Cr_{12}Gd_4}$} cluster shows the formation of rare closed, heptametallic species namely {$\mathbf{Cr_6Cu}$}, {$\mathbf{Cr_5Cu_2}$} and {$\mathbf{Cr_5Gd_2}$} as dominant products, as well as other closed ions like {$\mathbf{Cr_5Cu}$}, {$\mathbf{Cr_{10}Cu}$}, {$\mathbf{Cr_{12}Cu}$}, {$\mathbf{Cr_{10}}$}, {$\mathbf{Cr_{12}}$}, and {$\mathbf{Cr_6Gd_2}$}. The collision cross section of cyclic products and precursors has a linear correlation with ion mass, a relationship that does not hold for acyclic systems. Thus, ion mobility mass spectrometry can determine whether a candidate polymetallic complex exists as a closed or open structure. As these rings are non-trivial to synthesize individually in solution, we propose the presented workflow as a means to identify and characterise feasible target molecules.

Introduction

Tandem mass spectrometry (MS^2) involves isolation of target ions in the gas phase and their subsequent dissociation to smaller ions. The most common fragmentation method is collision-induced dissociation (CID), in which analytes are subjected to collisions with an inert gas at user-defined kinetic energies. The structure of newly formed products as well as non-fragmented precursor ions can be accessed when CID is combined with ion mobility mass spectrometry (IM-MS), which allows the mass as well as size and shape to be measured in the same experiment. Structural information is provided in the form of collision cross sections (*CCS*), which can be compared to literature data or to theoretical values computed from candidate geometries. Due to the high energies involved in collisional activation, analytes tend to disrupt and undergo major structural change, which becomes visible in the ion mobility spectra of the precursor and/or product ions. Particularly for proteins, the term "collision-induced unfolding" was coined to describe this behaviour similar to denaturation.[1] Although the disassembly of biomacromolecules is commonly investigated,[2–5] the impact of collisional activation on large synthetic molecules is not well explored.

We have been studying a family of cyclic polymetallic supramolecules proposed as qubits in quantum information processing;[6–9] related compounds have also been used as resists for lithography.[10–12] As the interest in these and other metallosupramolecular complexes increases, and similarly the complexity of their structures,[13–15] the synthesis and analysis of their building blocks could aid in rationalising the preference for certain compounds and predict the formation of others.

Perhaps the most prominent example where mass spectrometry was used to find a molecule stable enough to be produced in bulk phase was the discovery of the C_{60} buckminsterfullerene by Kroto *et al.* in 1985,[16] which led to the award of the Nobel Prize in Chemistry eleven years later.[17–19] More recently, Cronin and co-workers have used cryospray and ion mobility mass spectrometry to identify polyoxometalate targets for bulk synthesis[20–23] and to unravel their assembly mechanism.[21,23,24] We have recently applied CID and IM-MS to investigate the disassembly mechanisms and energetics of heterometallic rings and [2]-rotaxanes with the general formula $[NH_2RR'][\mathbf{Cr_7M}F_8(O_2C^tBu)_{16}]$ (M = Mn^{II}, Fe^{II}, Co^{II}, Ni^{II}, Cu^{II}, Zn^{II}, Cd^{II}), showing that both the metal M and the R, R' groups can be used to tune the stability and conformational dynamics of these systems.[25]

Here, we investigate the disassembly dynamics of more complex heterometallic systems, two of which have hourglass structures, $[NH_2{}^nPr_2]_2[\mathbf{Cr_{10}Cu_2}F_{14}(O_2C{}^tBu)_{22}]$ = "{$\mathbf{Cr_{10}Cu_2}$}" (Figure 1a) and $[NH_2{}^iPr_2]_2[\mathbf{Cr_{12}Cu_2}F_{16}(O_2C{}^tBu)_{24}]$ = "{$\mathbf{Cr_{12}Cu_2}$}" (Figure 1b), and a third which involves a lanthanide tetrahedron bound to two {$\mathbf{Cr_6}$} chains, $[NH_2{}^nPr_2]_2[\mathbf{Cr_{12}Gd_4}F_{21}(O_2C{}^tBu)_{29}]$ = "{$\mathbf{Cr_{12}Gd_4}$}" (Figure 1c). We demonstrate how CID, aided by IM-MS, can discriminate different disassembly pathways, which lead to the production of closed polymetallic species that have not been made previously *via* solution synthesis (Figure 1d). We suggest that this workflow could therefore inspire new synthetic targets and inform the tools available for the formation of metallosupramolecular compounds. Using information from the CID-IM-MS measurements, we also propose a workflow for the topological assignment of new polymetallic systems, which applies to structures synthesised in solution as well as those formed in the gas phase.

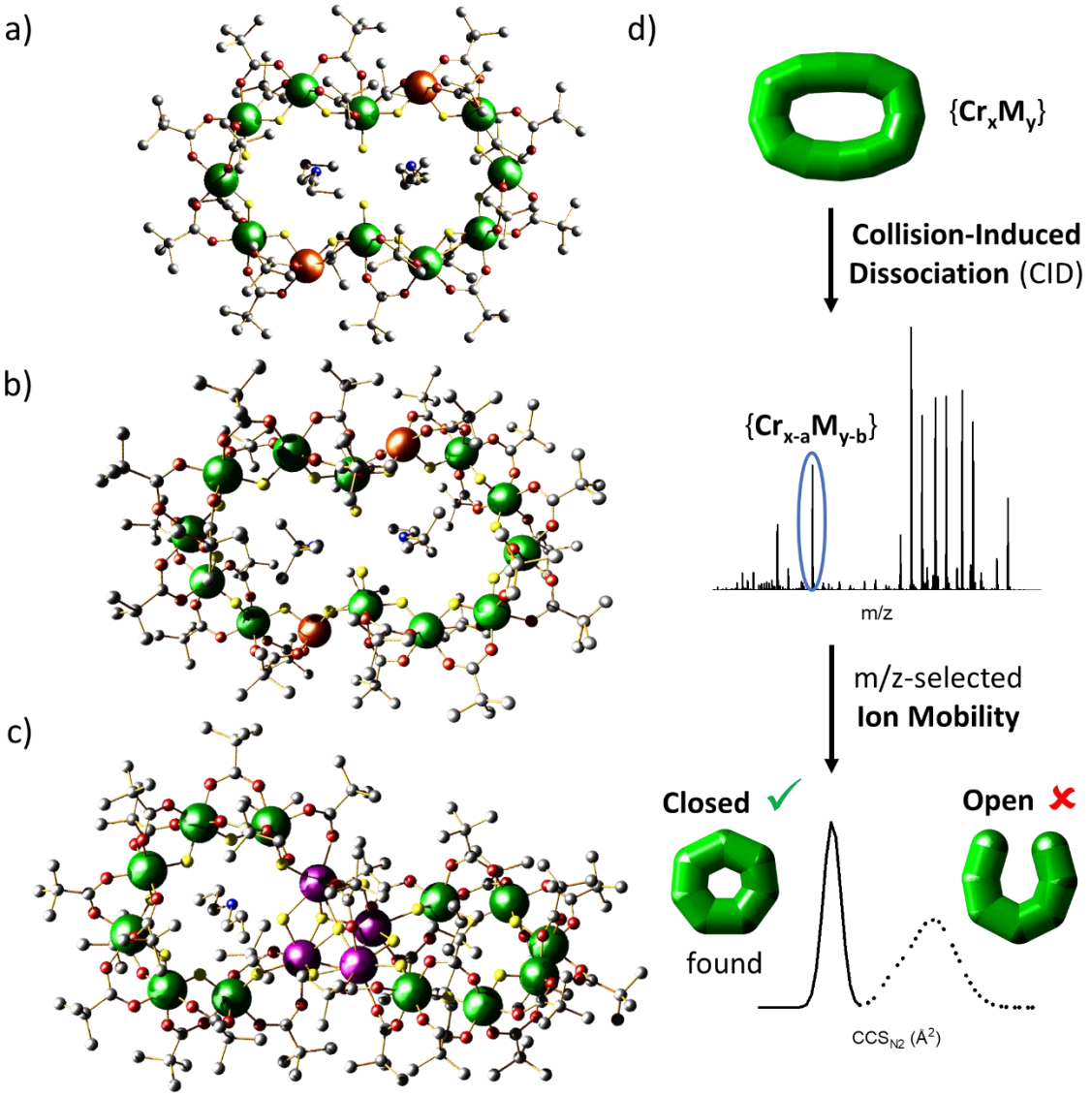

Figure 1: Single crystal X-ray structure of a) $\{Cr_{10}Cu_2\}$, b) $\{Cr_{12}Cu_2\}$[26] and c) $\{Cr_{12}Gd_4\}$; Cr: dark green, Cu: brown, Gd: purple, F: yellow, O: red, N: blue, C: grey). Solvent molecules and hydrogen atoms have been removed for clarity. d) CID-IM-MS workflow following nano-electrospray ionisation of the precursor $\{Cr_xM_y\}$ from solution and *m/z*-selection of an appropriate precursor ion. Upon collisional activation, several fragment ions are observed with different masses, and their CCS_{N2} distribution can be extracted as shown for an ion of the type $\{Cr_{x-a}M_{y-b}\}$. Different structures of $\{Cr_{x-a}M_{y-b}\}$ are possible, e.g. closed (low CCS_{N2}, narrow CCS_{N2} distribution) or open forms (high CCS_{N2}, wide CCS_{N2} distribution), of which only a closed $\{Cr_{x-a}M_{y-b}\}$ species was found in this illustrative example.

Results

{$Cr_{10}Cu_2$} and {$Cr_{12}Cu_2$} Hourglasses

The hourglass structures {$\mathbf{Cr_xCu_2}$} (x = 10, 12) consist of two $\mathbf{Cu^{II}}$ and x $\mathbf{Cr^{III}}$ centres, which are bridged *via* pivalate ligands ($^-O_2C^tBu$ = Piv^-) on the outside, and fluorides on the inside of the hourglass structure (Figure 1a and b). The coordination environment of the chromium ions involves four pivalates and two *cis*-fluorides with the exception of those located at the hourglass bottleneck, where three pivalates and three *mer*-fluorides are present. These centres are adjacent to the two copper ions, which are penta-coordinated by three pivalates and two fluorides. Additionally, one secondary ammonium cation is located in each half of the hourglass (for {$\mathbf{Cr_{10}Cu_2}$}: $[NH_2{}^nPr_2]^+$ and for {$\mathbf{Cr_{12}Cu_2}$}: $[NH_2{}^iPr_2]^+$), where it exhibits hydrogen bonds to the fluorides, particularly to the terminal fluorides attached to the two bottleneck chromiums.[26,27] Following optimization of solvent and nano-electrospray ionisation (nESI) source conditions, mass spectra of {$\mathbf{Cr_xCu_2}$} (x = 10, 12) were recorded from solutions of sodium iodide in positive mode. Cations of the type [{$\mathbf{Cr_xCu_2}$} + $Na]^+$ were obtained for both hourglasses (Figures S1, S2).

Disassembly of {$\mathbf{Cr_{10}Cu_2}$} and {$\mathbf{Cr_{12}Cu_2}$}. We isolated the ions [{$\mathbf{Cr_{10}Cu_2}$} + $Na]^+$ and [{$\mathbf{Cr_{12}Cu_2}$} + $Na]^+$ and ramped the energy of collisional activation with nitrogen gas, whilst recording the arrival time distributions (*ATD*) of both analytes and their products. The *ATD* of all ions were converted to CCS_{N2} distributions as a function of collision energy. The tandem mass spectra (MS^2) of both precursor ions show the loss of one secondary ammonium cation along with an anionic ligand, predominantly a pivalate, as the first dissociation step (Figure 2). E_{50} values, known as a relative measure of ion stability, were determined for both precursor ions and show a slightly higher stability for [{$\mathbf{Cr_{12}Cu_2}$} + $Na]^+$ (Figure S3).

Accurate mass and isotopic distributions were used to assign the hourglass fragments in the subsequent dissociation steps at higher collision energies. A variety of dissociation channels occur and ions are observed in two regions of the mass spectrum, one at lower *m/z* (x = 10: < 1800 *m/z*; x = 12: < 2200 *m/z*) and one at higher *m/z* (x = 10: 2500 – 3200 *m/z*; x = 12: 2000 – 3700 *m/z*). All of the observed species are singly charged cations, and between these two regions only minor ion populations were found (Figure 2). For [{$\mathbf{Cr_{12}Cu_2}$} + $Na]^+$, more ions were found in the low mass region compared to [{$\mathbf{Cr_{10}Cu_2}$} + $Na]^+$, for which the high mass

region clearly dominates. The ratio between the precursor and product ions in both regions depends both on the collision energy (Figure 2) and the instrument used (Figure S4).

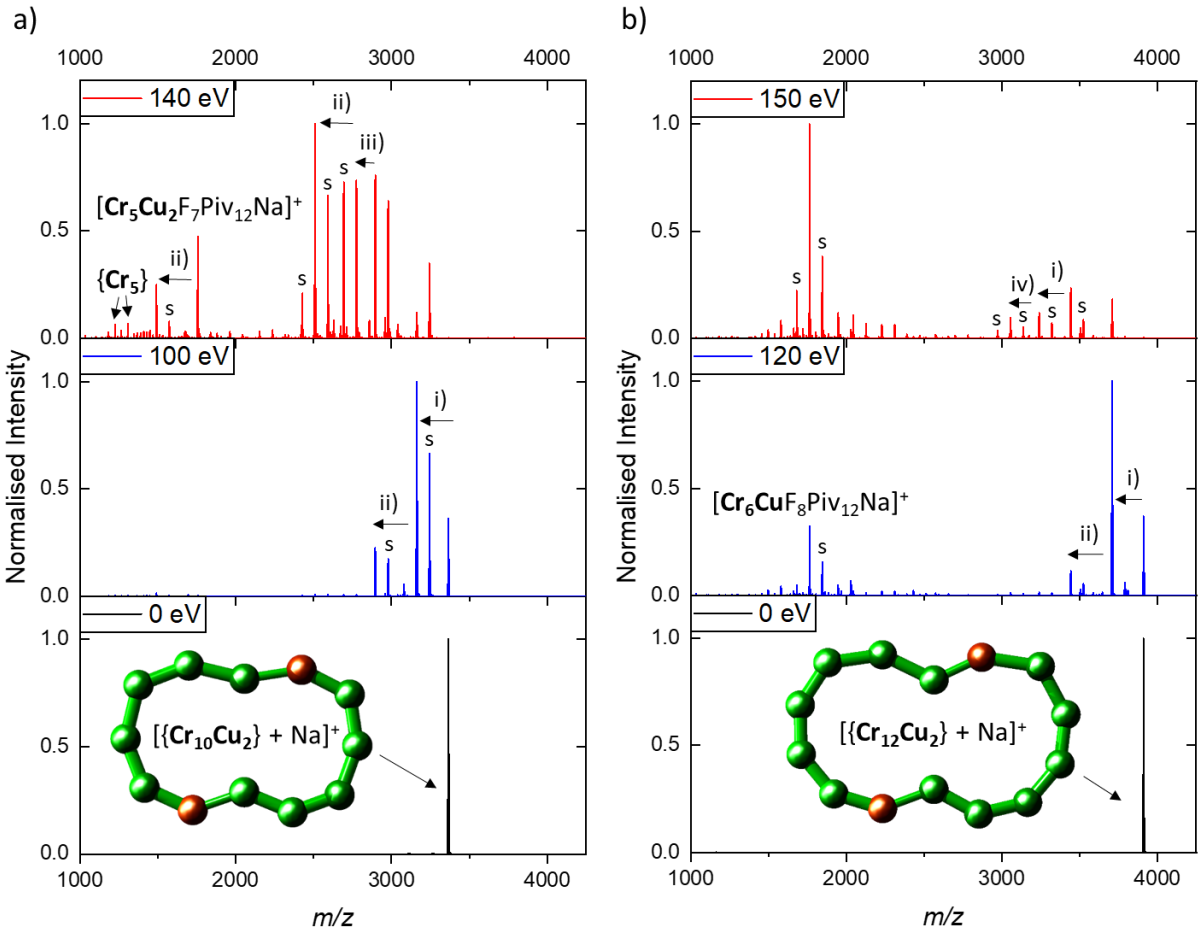

Figure 2: Tandem Mass Spectra of a) [{**Cr$_{10}$Cu$_2$**} + Na]$^+$ (*m/z* = 3365) at collision energies of 0 eV, 100 eV and 140 eV and b) [{**Cr$_{12}$Cu$_2$**} + Na]$^+$ (*m/z* = 3910) at collision energies of 0 eV, 120 eV and 150 eV. Occurring fragmentation pathways are labelled: i) – [$NH_2^{n/i}Pr_2$]$^+$, – Piv$^-$; ii) – **Cu^{II}**, – 2 Piv$^-$; iii) – [$NH_2^{n/i}Pr_2$]$^+$, – F$^-$ and iv) – **Cu^{II}**, – Piv$^-$, – F$^-$. Satellite peaks (labelled with "s") correspond to the labelled main peak *via* the exchange of one anionic ligand for another one (Piv$^-$ for F$^-$ or F$^-$ for Piv$^-$; mass difference = 82 Da). The spectra of both ions present two regions, one at lower *m/z* and one at higher *m/z*. Insets: Schematics of {**Cr$_{10}$Cu$_2$**} and {**Cr$_{12}$Cu$_2$**} (Cr: green, Cu: brown).

The dominant fragment ions of the low mass region contain seven transition metal ions. From the precursor [{**Cr$_{10}$Cu$_2$**} + Na]$^+$, it is {**Cr$_5$Cu$_2$**} (mainly [**Cr$_5$Cu$_2$**F$_7$Piv$_{12}$Na]$^+$ at 1756 *m/z*). We also observe in minor amounts {**Cr$_5$**} that likely is the other direct fragment of the {**Cr$_{10}$Cu$_2$**} dissociation, at least partially (Figure 2a top and Supplementary Dataset). {**Cr$_5$Cu**} was also

found in low numbers (mainly [**Cr$_5$Cu**F$_7$Piv$_{10}$Na]$^+$ at 1491 *m/z*), however this, and other low abundance ions, are presumably secondary fragment from {**Cr$_5$Cu$_2$**} as they appear at higher energies than the latter (for {**Cr$_5$Cu**}: loss of **Cu^{II}** and two Piv$^-$, Figure 2a). In contrast, the precursor [{**Cr$_{12}$Cu$_2$**} + Na]$^+$ dissociates to {**Cr$_6$Cu**} (mainly [**Cr$_6$Cu**F$_8$Piv$_{12}$Na]$^+$ at 1764 *m/z*, Figure 2b). The species in the high mass region follow fragmentation channels where **Cu^{II}** dissociates along with two anionic ligands, before the second ammonium cation and another ligand are lost. This in turn is followed by the dissociation of the second **Cu^{II}** centre, again along with two anionic ligands (Figure 2). Overall, this yields species of the type **Cr$_x$** (x = 10, 12) as the product ions of the hourglass ions [{**Cr$_x$Cu$_2$**} + Na]$^+$, which was confirmed by their isotopic distributions as illustrated for [**Cr$_{12}$**F$_{15}$Piv$_{21}$Na]$^+$ (m/z = 3056, Figure S5).

Ion mobility allows us to probe the structure of both precursor and product ions *via* their *CCS$_{N2}$* distributions (Figure 3). The majority of products exhibit narrow, unimodal conformations, although slightly wider distributions were found for {**Cr$_{12}$Cu**} and {**Cr$_{12}$**} fragment ions of [**Cr$_{12}$Cu$_2$** + Na]$^+$ (Figure 3b) as well as for some {**Cr$_5$**} species formed in the disassembly of [{**Cr$_{10}$Cu$_2$**} + Na]$^+$ (Supplementary Dataset). The *CCS$_{N2}$* values of the hourglass precursor ions and the presented products were quantified and compared with data of similar polymetallic closed species (Table 1). The data for {**Cr$_5$Cu$_2$**} and {**Cr$_6$Cu**} agree well with the *CCS$_{N2}$* of a seven-membered [**Cr$_6$Mn**F$_8$Piv$_{13}$]$^-$ ring, formed from a {**Cr$_7$Mn**} ring *via* CID-MS,[25] and the small difference can be explained with the different number of bulky pivalate ligands ({**Cr$_5$Cu$_2$**}, {**Cr$_6$Cu**}: 12 Piv$^-$, {**Cr$_6$Mn**}: 13 Piv$^-$). This, and their unimodal, narrow distributions clearly suggest a limited conformational flexibility and hence the presence of heptametallic {**Cr$_5$Cu$_2$**} and {**Cr$_6$Cu**} species that are closed, which is distinct from other open {**Cr$_6$Mn**} horseshoe fragments observed previously (Table 1).[25] Other products and precursor ions cannot be directly compared to previous data, however their only slightly different *CCS$_{N2}$* values and similarly unimodal and narrow peak shapes indicate cyclic structures as well for these species (Figure 3, Supplementary Dataset). For the minor {**Cr$_5$**} fragments, depending on the exact chemical composition of the cations, the conformational landscape is more diverse (Supplementary Dataset).

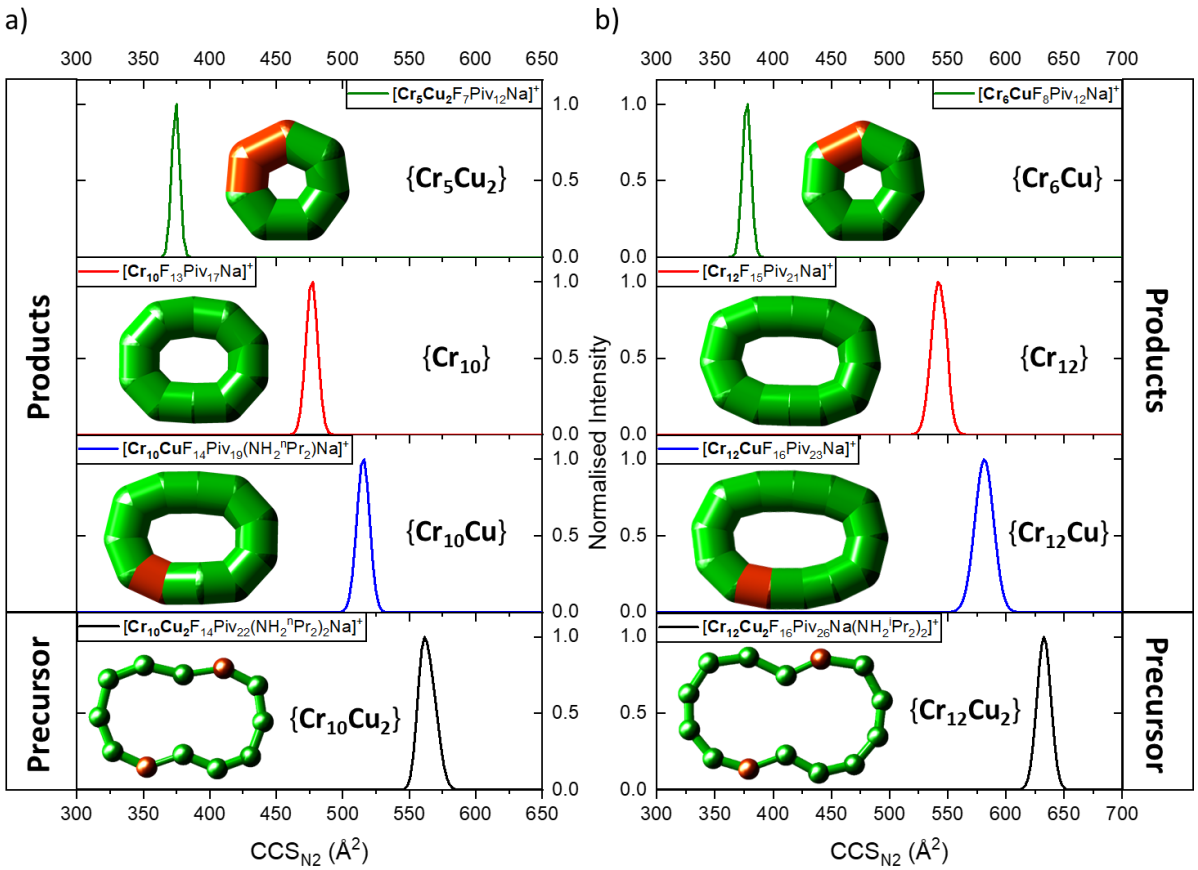

Figure 3: *CCS$_{N2}$* Distributions of a) [{**Cr$_{10}$Cu$_2$**} + Na]$^+$ (m/z = 3365) including selected product ions of the types {**Cr$_{10}$Cu**} (m/z = 2896), {**Cr$_{10}$**} (m/z = 2509), {**Cr$_5$Cu$_2$**} (m/z = 1756), and b) [{**Cr$_{12}$Cu$_2$**} + Na]$^+$ (m/z = 3910) including selected product ions of the types {**Cr$_{12}$Cu**} (m/z = 3443), {**Cr$_{12}$**} (m/z = 3056), {**Cr$_6$Cu**} (m/z = 1764). Data were recorded at collision energies of 0 eV (both precursor ions) as well as 120 eV (fragments of [{**Cr$_{10}$Cu$_2$**} + Na]$^+$) and 160 eV (fragments of [{**Cr$_{10}$Cu$_2$**} + Na]$^+$), respectively. Insets: Schematics of {**Cr$_{10}$Cu$_2$**}, {**Cr$_{12}$Cu$_2$**} and their products (Cr: green, Cu: brown). Fragment ions that are assigned closed due to the ion mobility data are presented schematically; the IM-MS experiment informs on the stoichiometry but not on the exact connectivity between the metal centres.

Table 1: $^{TW}CCS_{N2}$ values of [{**Cr$_{10}$Cu$_2$**} + Na]$^+$, [{**Cr$_{12}$Cu$_2$**} + Na]$^+$ and [{**Cr$_{12}$Gd$_4$**} – Piv]$^+$ including selected product ions. $^{TW}CCS_{N2}$ values of other structures were added from our previous works for comparisons.[25,28] Data shown represents different collision energies, which can lead to small deviations. For both types of {**Cr$_6$Mn**} horseshoes (i.e. open chains), the broad $^{TW}CCS_{N2}$ distributions were fitted with two Gaussian distributions, and their two maxima are noted in the table.

Source	Cluster Type	Composition	*m/z*	$^{TW}CCS_{N2}$ (Å^2)
Disassembly of [{**Cr$_{10}$Cu$_2$**} + Na]$^+$	{**Cr$_{10}$Cu$_2$**}	[**Cr$_{10}$Cu$_2$**F$_{14}$Piv$_{22}$(NH$_2$^{n}Pr$_2$)$_2$Na]$^+$	3365	566.5 ± 0.6
	{**Cr$_{10}$Cu**}	[**Cr$_{10}$Cu**F$_{14}$Piv$_{19}$(NH$_2$^{n}Pr$_2$)Na]$^+$	2896	514.1 ± 1.3
	{**Cr$_{10}$**}	[**Cr$_{10}$**F$_{13}$Piv$_{17}$Na]$^+$	2509	476.0 ± 0.8
	{**Cr$_5$Cu$_2$**}	[**Cr$_5$Cu$_2$**F$_7$Piv$_{12}$Na]$^+$	1756	374.2 ± 0.2
	{**Cr$_5$Cu**}	[**Cr$_5$Cu**F$_7$Piv$_{10}$Na]$^+$	1491	348.9 ± 0.1
Disassembly of [{**Cr$_{12}$Cu$_2$**} + Na]$^+$	{**Cr$_{12}$Cu$_2$**}	[**Cr$_{12}$Cu$_2$**F$_{16}$Piv$_{26}$(NH$_2$^{i}Pr$_2$)$_2$Na]$^+$	3910	633.2 ± 0.6
	{**Cr$_{12}$Cu**}	[**Cr$_{12}$Cu**F$_{16}$Piv$_{23}$(NH$_2$^{i}Pr$_2$)Na]$^+$	3443	580.2 ± 1.3
	{**Cr$_{12}$**}	[**Cr$_{12}$**F$_{15}$Piv$_{21}$Na]$^+$	3056	541.9 ± 0.3
	{**Cr$_6$Cu**}	[**Cr$_6$Cu**F$_8$Piv$_{12}$Na]$^+$	1764	376.3 ± 1.0
Disassembly of [{**Cr$_{12}$Gd$_4$**} – Piv]$^+$	{**Cr$_{12}$Gd$_4$**}	[**Cr$_{12}$Gd$_4$**F$_{21}$Piv$_{28}$(NH$_2$^{n}Pr$_2$)$_2$]$^+$	4688	703.5 ± 6.3
	{**Cr$_6$Gd$_2$**}	[**Cr$_6$Gd$_2$**F$_8$Piv$_{16}$(NH$_2$^{n}Pr$_2$)]$^+$	2499	446.1 ± 0.1
	{**Cr$_5$Gd$_2$**}	[**Cr$_5$Gd$_2$**F$_8$Piv$_{12}$]$^+$	1940	377.4 ± 0.7
Literature Values	{**Cr$_8$**}	[**Cr$_8$**F$_8$Piv$_{16}$Na]$^+$	2208	430.0 ± 0.8
	{**Cr$_7$Cu**}	[**Cr$_7$Cu**F$_8$Piv$_{16}$]$^-$	2197	432.7 ± 2.0
	{**Cr$_6$Mn**} Closed	[**Cr$_6$Mn**F$_7$Piv$_{14}$]$^-$	1915	401.5 ± 0.1
		[**Cr$_6$Mn**F$_8$Piv$_{13}$]$^-$	1833	394.2 ± 0.1
	{**Cr$_6$Mn**} Open Horseshoe	[**Cr$_6$Mn**F$_7$Piv$_{14}$]$^-$	1915	429.3 ± 0.1 and 444.3 ± 0.1
		[**Cr$_6$Mn**F$_8$Piv$_{13}$]$^-$	1833	413.4 ± 0.1 and 426.9 ± 0.1

{$Cr_{12}Gd_4$} Cluster

We further investigated whether collision-induced disassembly would also lead to polymetallic rings when activating a different type of precursor. We chose the lanthanide cluster {**$Cr_{12}Gd_4$**} (Figure 1c), which consists of a tetrahedral {**Gd_4**F_7Piv} cage, in which the fluorides and one pivalate bridge the four **Gd^{III}** centres. Each of the octa-coordinated gadolinium ions is attached to a terminus of one of two {**Cr_6**} chains, and a $[NH_2{}^nPr_2]^+$ cation is located at each ring centre.[29] The chromium atoms are each connected *via* two pivalate ligands and one fluoride, as in both {**Cr_xCu_2**} hourglasses.

The mass spectrum of {**$Cr_{12}Gd_4$**}, sprayed from methanol in the presence of sodium iodide using nESI, yielded only a small number of largely intact analyte ions (Figure S6), and we assigned the dominant one to [{**$Cr_{12}Gd_4$**} – Piv]$^+$ (*m/z* = 4688, Figure S7 for Isotopic Distribution). Several other polymetallic species were observed in the mass spectrum, including {**Cr_6Gd**} ions, which are possibly produced by decomposition reactions with the solvent. Using ion mobility, the {**Cr_6Gd**} clusters were identified as heptametallic rings (CCS_{N2} values in Table S1 including discussion of their disassembly; Supplementary Dataset), which are isostructural to a {**Cr_6Ce**} ring reported previously, which was only synthesised in very low yield (see Discussion).[29] We computed the DFT optimised structure of the neutral {**Cr_6Gd**} (Figure S8) as well as the corresponding sodium adduct (Supplementary Dataset), supporting their stabilities in the gas phase.

*Disassembly of {**$Cr_{12}Gd_4$**}.* We used the tandem mass spectrometry ion mobility workflow (Figure 1d) to study [{**$Cr_{12}Gd_4$**} – Piv]$^+$. Similar to the studies of [{**Cr_xCu_2** + Na]$^+$, the tandem mass spectra show the loss of $[NH_2{}^nPr_2]^+$ along with one fluoride as the main fragmentation channel, although at higher energies (Figure 4a). The E_{50} value of [{**$Cr_{12}Gd_4$**} – Piv]$^+$ was determined and is more than 50% higher than those of the hourglass ions (Figure S9). Upon increasing the energy further (Figure 4a centre), two main regions were found in the tandem mass spectra: one at 1800 - 2500 *m/z* and the other at 3200 – 4500 *m/z*, however the separation between regions is blurred at higher collision energies (Figure 4a top). All species also occur as singly charged cations. In the lower mass region, the cluster type {**Cr_6Gd_2**} was found as the main product (mainly [**Cr_6Gd_2**$F_8Piv_{16}(NH_2{}^nPr_2)]^+$ at *m/z* = 2499, Figure S10 for Isotopic Distribution). This cluster is one half of the {**$Cr_{12}Gd_4$**} precursor and we previously reported the solid-state structure of a cyclic {**Cr_6Y_2**} complex, albeit in low yield.[14] The {**Cr_6Gd_2**}

ions undergo further fragmentation at even higher energies, with losses of $[NH_2{}^nPr_2]^+$ or **Cr^{III}**, along with anionic ligands (mainly pivalates, Figure 4a bottom). This for example leads to ions of the type {**Cr$_5$Gd$_2$**} (e.g. [**Cr$_5$Gd$_2$**F$_8$Piv$_{12}$]$^+$ at *m/z* = 1940). In contrast, the high mass region shows the stepwise disruption of the {**Cr$_6$**} chains with losses of $[NH_2{}^nPr_2]^+$ along with Piv$^-$, followed by several dissociations of {**Cr**(Piv)$_3$} units (Figure 4a centre). This infers that the {**Gd$_4$**} tetrahedron remains intact.

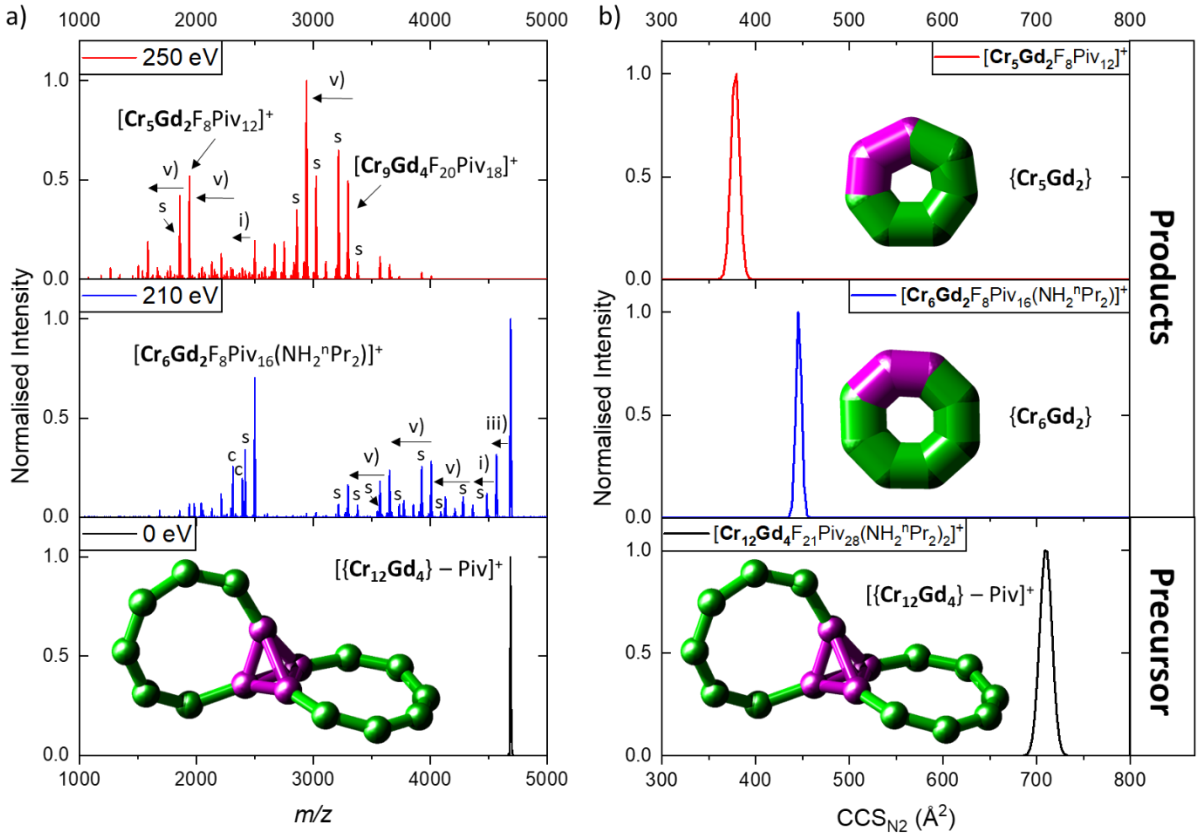

Figure 4: a) Tandem Mass Spectra of [{**Cr$_{12}$Gd$_4$**} – Piv]$^+$ at collision energies of 0 eV, 210 eV and 250 eV. Occurring fragmentation pathways are labelled: i) – $[NH_2{}^{n/i}Pr_2]^+$, – Piv$^-$; iii) – $[NH_2{}^{n/i}Pr_2]^+$, – F$^-$ and v) – **Cr^{III}**, – 3 Piv$^-$. Satellite peaks (labelled with "s") correspond to the labelled main peak *via* the exchange of one anionic ligand for another one (Piv$^-$ for F$^-$ or F$^-$ for Piv$^-$; mass difference = 82 Da). The spectrum at 210 eV shows two regions, one at lower *m/z* and one at higher *m/z*. Minor contaminant features were observed which were *m/z*-selected in the quadrupole along with [{**Cr$_{12}$Gd$_4$**} – Piv]$^+$, and hence produce different fragments (labelled with "c"). b) *CCS$_{N2}$* Distributions of [{**Cr$_{12}$Gd$_4$**} – Piv]$^+$ (m/z = 4688) and the fragment ions {**Cr$_6$Gd$_2$**} (m/z = 2499) and {**Cr$_5$Gd$_2$**} (m/z = 1940). Data were recorded at collision energies of 0 eV (precursor), 130 eV for {**Cr$_6$Gd$_2$**} and 190 eV for {**Cr$_5$Gd$_2$**}, respectively. Insets:

Schematics of {**Cr$_{12}$Gd$_4$**} and the two products {**Cr$_x$Gd$_2$**} (x = 5, 6; **Cr**: green, **Gd**: purple). Fragment ions that are assigned closed due to the ion mobility data are presented schematically; the IM-MS experiment informs on the stoichiometry but not on the exact connectivity between the metal centres.

The structure of [{**Cr$_{12}$Gd$_4$**} – Piv]$^+$ and fragment ions was investigated via their *CCS$_{N2}$* distributions (Figure 4b for selected ions). The majority of the ions exhibit narrow, unimodal conformations (Supplementary Dataset). We quantified absolute *CCS$_{N2}$* values of the precursor [{**Cr$_{12}$Gd$_4$**} – Piv]$^+$ and products of the type {**Cr$_6$Gd$_2$**} and {**Cr$_5$Gd$_2$**} (Table 1). The *CCS$_{N2}$* value of {**Cr$_6$Gd$_2$**} agrees well with a related {**Cr$_7$Cu**} ring,[25] while the value for {**Cr$_5$Gd$_2$**} is similar to those of the seven-membered hourglass products {**Cr$_5$Cu$_2$**} and {**Cr$_6$Cu**}**,** as well as to the [**Cr$_6$Mn**F$_8$Piv$_{13}$]$^-$ closed species.[25] These comparisons suggest closed, cyclic structures for the complexes of the type {**Cr$_6$Gd$_2$**} and {**Cr$_5$Gd$_2$**}.

Density Functional Theory and Collision Cross Section Calculations

To assess the stability of the closed fragments formed in the disassembly of {**Cr$_{10}$Cu$_2$**}, {**Cr$_{12}$Cu$_2$**} and {**Cr$_{12}$Gd$_4$**}, DFT optimised structures were generated for {**Cr$_5$Cu$_2$**}, {**Cr$_5$Cu**}, {**Cr$_6$Cu**}, {**Cr$_6$Gd$_2$**} and {**Cr$_5$Gd$_2$**} (Figures S11 – S15). At the level of theory used, all closed cations are considerably more stable with respect to their monometallic fragments [**Cr**FPiv$_2$], [**Cr**F$_2$Piv], [**Cu**FPiv$_2$]$^-$, [**Cu**F$_2$Piv]$^-$ and Piv$^-$, by at least 1400 kJ/mol. For the heptametallic species {**Cr$_5$Cu$_2$**}, {**Cr$_6$Cu**} and {**Cr$_5$Gd$_2$**}, different isomers were calculated, and the DFT energies suggest that hexametallic rings involving an additional metal bridge might even be more stable than the corresponding heptametallic rings (Figures S11, S13 and S15, Supplementary Dataset). We cannot assign the observed fragments unambiguously to the computed candidate structures since the kinetics of the dissociation reaction and its mechanism are unknown; in addition our sampling of candidate structures is not exhaustive.

Theoretical TH*CCS$_{N2}$* values were enumerated for {**Cr$_5$Cu**} and {**Cr$_6$Gd$_2$**} as well as the different isomers of {**Cr$_5$Cu$_2$**}, {**Cr$_6$Cu**} and {**Cr$_5$Gd$_2$**}, using the trajectory method implemented in IMoS.[30] This yielded 3-8% larger values than found experimentally (Table S2), and we previously observed this discrepancy for similar polymetallic complexes,[25,28] and have discussed possible explanations in detail.[25] An exception to this was found for the six-membered ring {**Cr$_5$Cu**}, where the experimental and theoretical *CCS$_{N2}$* values are in good agreement. The reason for

this is not known but given that this is the most compact and dense structure (Figure S12), it suggests that the cavities in the larger rings are not well represented by the computational $^{TH}CCS_{N2}$ methodology with the trajectory method, as previously discussed.[25] The $^{TH}CCS_{N2}$ values of the different heptametallic isomers {**Cr_5Cu_2**}, {**Cr_6Cu**} and {**Cr_5Gd_2**} are similar (Table S2), and the fragment structures can hence not be resolved *via* comparisons of experimental and theoretical CCS_{N2}.

We examined the high mass loss from {**$Cr_{10}Cu_2$**} in more detail. Experiment suggests that the cleavage does not occur at the hourglass bottleneck, as observed for {**$Cr_{12}Cu_2$**} and resulting in {**Cr_6Cu**}, but counterintuitively at the adjacent Cr-Cu edge. This leads to the formation of {**Cr_5Cu_2**} instead of {**Cr_5Cu**}, which is in agreement with the thermodynamic stabilities of the DFT optimised structures (Figures S11 and S12, Supplementary Dataset). Here, the disassembly of {**Cr_5Cu_2**} → {**Cr_5Cu**} + [**Cu**Piv_2] is endothermic (ΔE ≈ 334 kJ/mol), and this fragmentation channel is experimentally only observed at higher collision energies (Figure 2a top).

Discussion

The first major finding from this work is the formation, separation and isolation of closed cyclic products in the gas phase from the collision-induced dissociation of the {**Cr_xCu_2**} hourglasses (x = 10, 12) and from {**$Cr_{12}Gd_4$**}. The observation that polymetallic rings are formed from all three precursors suggests that this workflow can produce smaller rings of varying sizes, including new types (see below), as long as appropriate larger precursors are available. Remarkable is that these rings form after collisions on a millisecond timescale, which suggests that both rearrangements and new bond formations occur fast. Also noteworthy is the occurrence of gaps in the tandem mass spectra of all three parent ions (Figures 2, 4a), which suggests that potential products in these regions are significantly less stable than those obtained at both lower and higher masses, akin to the magic numbers seen in the spectra for monatomic and molecular cluster ions.[16,31–35] For the low *m/z* region, the primary and kinetically most stable products from the precursor ions are {**Cr_5Cu_2**}, {**Cr_6Cu**} and {**Cr_6Gd_2**}, whereas others such as {**Cr_5Cu**} and {**Cr_5Gd_2**} are secondary products from these fragments.

Particularly striking is the formation of the closed, heptametallic species {**Cr_5Cu_2**}, {**Cr_6Cu**} and {**Cr_5Gd_2**}, for which DFT optimisations indicate several plausible structures (Figures S11, S13

and S15). In all three cases, the lowest energy conformer of those sampled involves a hexametallic ring with an additional metal bridge. In the family of polymetallic chromium rings,[36] the only closed seven-metal ring synthesized to date is {**Cr$_6$Ce**}, which only forms as a very minor side product,[29] and this is one of three structurally characterised heptametallic rings known.[37,38] Given the sparsity of known heptametallic compounds it might be argued that these products are unlikely, however in the synthesis of heterometallic chromium rings the difficulty is avoiding the formation of [**Cr$_8$**F$_8$Piv$_{16}$], which is achieved by adding a cationic template that occupies the centre of the cavity and leads to an anionic heterometallic ring.[27] This allows formation of larger rings by choice of larger templates, but for closed seven-metal species there is insufficient space for any organic template. Applying the presented CID-MS approach on these larger complexes therefore offers a new route for the formation of closed heptametallic and smaller species, and we have confirmed their gas phase stability using DFT.[25]

The discussed approach can inspire new supramolecular chemistry outside the gas phase. In some cases, rings similar to those produced by CID-MS have been previously synthesised and characterised. For example, several {**Cr$_{10}$**} rings have been reported by our group, however these involved different bridging ligands.[39–41] We have also structurally characterised a {**Cr$_6$Y$_2$**} ring of the formula [**Cr$_6$Y$_2$**F$_8$Piv$_{17}$(NH$_2$Et$_2$)(H$_2$O)], which is highly similar to the ion [**Cr$_6$Gd$_2$**F$_8$Piv$_{16}$(NH$_2$^{n}Pr$_2$)]$^+$ observed upon fragmentation of {**Cr$_{12}$Gd$_4$**}. The {**Cr$_6$Y$_2$**} was formed only in low yield which correlates with the observation that the solution synthesis leads to {**Cr$_{12}$Ln$_4$**} cages as the major products.[29]

Another aim for future endeavours is to connect gas phase experiments with bulk phase *via* the so-called preparative mass spectrometry ("ion soft-landing"), in which ions produced in the mass spectrometer are transferred and gently deposited on a surface.[42–44] This surface can in turn be analysed by a range of microscopy[45,46], spectroscopy[47,48] or mass spectrometry techniques[49], among others. As the field of soft-landing is still in its infancy and rapidly evolving, we hypothesise that the presented CID-MS formation strategy will be of practical significance for synthetic chemists in the future.

Our second major observation is that ion mobility can be used to identify whether a given polymetallic complex of this family is cyclic or not, and this applies both to structures formed *via* CID-MS in the gas phase, and also to those synthesised in solution that are just transferred to the gas phase (e.g. {**$Cr_{10}Cu_2$**}, {**$Cr_{12}Cu_2$**} and {**$Cr_{12}Gd_4$**}). The two main advantages here, compared to other bulk phase methods, are small measurement times and low amounts of samples needed. When directly assigning structures using ion mobility, theoretical calculations such as DFT are commonly applied to compare theoretical *CCS* values to those found experimentally, however this can be non-trivial and requires careful structural and conformational sampling. Based on DFT calculations, we have benchmarked the following workflow to theoretical CCS_{N2} values from this and previous works, yielding good agreement.[25,28]

We plot the CCS_{N2} of all species examined here and from previous work (Table 1) against their adjusted masses (Figure 5). This correlation represents the atom density in a given ion,[50–52] which is highest for ions with small *CCS* and large mass. Previously, Bleiholder *et al.* tracked the self-assembly of peptides and, using an analogous relationship, distinguished between the formation of larger globular peptides and β-sheets relevant for amyloid fibril formation.[51] Later our group showed that the *CCS*/*m* slope of unfolded and intrinsically disordered proteins is significantly higher (lower density) than for native proteins.[52] In the case of cyclic species from this and previous works, we observe a linear correlation, which does not hold for the acyclic {**$Cr_{12}Gd_4$**} cluster and the extended {**Cr_6Mn**} horseshoes.[25] These are located above the line as their estimated spherical densities (ESD) are lower than for the polymetallic cyclic structures (Figure 5 Inset). ESD were derived from CCS_{N2} values, following previously published calculations based on the assumption of a spherical ion,[50] and cannot be directly compared to the macromolecular density in the crystal structures, where available. The latter is typically higher (1.2 – 1.4 g/cm^3) and represents the packing density of the molecules in the crystal lattice (together with solvent molecules), whereas the ESD discussed here inform on how dense the atoms are in the gas phase ion.

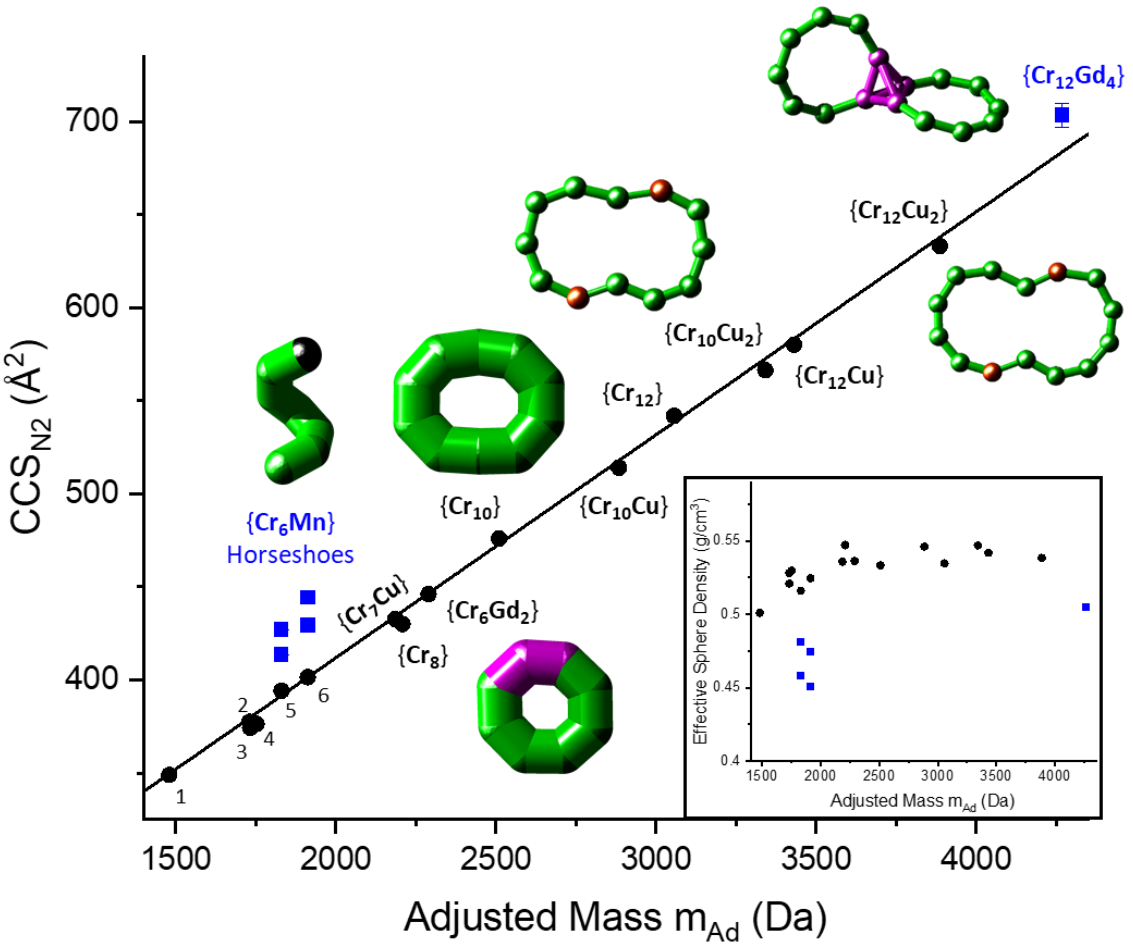

Figure 5: Correlation between CCS_{N2} and adjusted mass m_{ad} for all species in Table 1. The cyclic complexes show a linear correlation, which does not hold for the acyclic ions ({**Cr$_{12}$Gd$_4$**} and {**Cr$_6$Mn**} horseshoes). 1: {**Cr$_5$Cu**}; 2: {**Cr$_5$Gd$_2$**}; 3: {**Cr$_5$Cu$_2$**}; 4: {**Cr$_6$Cu**}; 5, 6: {**Cr$_6$Mn**} rings. The mass was adjusted so that every metal centre is accounted for with the mass of chromium (52 Da). This model is reasonable as the nature of the metal in the polymetallic complex has a low overall impact on the CCS_{N2}, although some have high masses, e.g. in the case of Gd. Inset: Schematics of selected cyclic and acyclic complexes (Cr: green, Cu: brown, Gd: purple, Mn: black). Fragment ions that are assigned closed due to the ion mobility data are presented schematically; the IM-MS experiment informs on the stoichiometry but not on the exact connectivity between the metal centres. Effective sphere density (ESD) derived from CCS_{N2} values *vs* adjusted mass (black circles: cyclic, blue squares: acyclic), showing that the acyclic {**Cr$_6$Mn**} horseshoes and {**Cr$_{12}$Gd$_4$**} have a lower ESD than the cyclic species.

*Disassembly of {**Cr$_{10}$Cu$_2$**} and {**Cr$_{12}$Cu$_2$**}.* The first dissociation step of both hourglass ions [{**Cr$_x$Cu$_2$**} + Na]$^+$ (x = 10, 12) is the loss of the secondary ammonium cation, along with an anionic ligand, predominantly a pivalate. This is probably because the cation is the only non-

covalently bound species in the system. As the primary fragmentation pathway is the same for both [{**Cr$_x$Cu$_2$**} + Na]$^+$ ions, their E_{50} values are also similar. The same dissociation channel was observed for the heterometallic rotaxanes [NH_2RR'][**Cr$_7$M**F_8Piv$_{16}$], where R and R' include bulky phenyl and *tert*-butyl groups.[25] The secondary ammonium cations are smaller here, so the relatively ease of dissociation from the hourglass ions is not surprising.

The further disassembly can be rationalised by considering the sites in the hourglass structure that are most prone to collision-induced dissociation. These are the two **Cu**^{II} centres and their ligands, because of the lower oxidation state (**Cu^{II}** vs. **Cr^{III}**), and hence a weaker electrostatic attraction between ligand and metal, as well as the coordination number (**Cu^{II}**: 5, **Cr^{III}**: 6, Figure 1a, b). It seems likely that both the initially lost ammonium cation and pivalate are adjacent to the same **Cu^{II}** centre. This would weaken the hourglass scaffold further in this region, which is the reason for its disruption in the second dissociation step (rather than the loss of the second ammonium cation). As discussed above, the hourglass disruption occurs *via* different pathways, yielding product ions either with low *m/z* or high *m/z*. It is also possible that some initial fragments at high *m/z* fragment further to smaller products.

Fragmentation associated with higher mass loss leads to rings of the type {**Cr$_5$Cu$_2$**} (from [{**Cr$_{10}$Cu$_2$**} + Na]$^+$) and {**Cr$_6$Cu**} (from [{**Cr$_{12}$Cu$_2$**} + Na]$^+$, Figures 2, 3 and Table 1). In the disassembly of {**Cr$_{12}$Cu$_2$**} the dissociation occurs at the hourglass bottleneck, and this is likely the favoured site as **Cu^{II}** is far more reactive than **Cr^{III},** and only two bridging ligands are present. As a result, the hourglass predominantly dissociates symmetrically to {**Cr$_6$Cu**}, which likely rearranges to a closed structure. For the fragmentation of {**Cr$_{10}$Cu$_2$**}, this same mechanism would lead to a six-membered {**Cr$_5$Cu**} species, but interestingly this ring, characterised by ion mobility, is only seen at higher energies. This suggests that it is a secondary fragment (Figure 2a and Supplementary Dataset). By contrast, we predominantly observe {**Cr$_5$Cu$_2$**} products due to an asymmetric hourglass disruption, and here three bonds need to be broken instead of two. This preference may be due to the stability given by the formation of the heptametallic species, which implies it is more stable than the alternative hexametallic {**Cr$_5$Cu**}. The comparison of their energetics using DFT supports these findings, showing that {**Cr$_5$Cu$_2$**} is the thermodynamically more stable product than {**Cr$_5$Cu**} ($\Delta E \approx 334$ kJ/mol; Figures S11, S12). Hence, the secondary, and endothermic disassembly from {**Cr$_5$Cu$_2$**} to {**Cr$_5$Cu**} and [**Cu**Piv_2] only occurs at higher collision energies. Notably, the lowest energy

isomer found for {**Cr$_5$Cu$_2$**} is a {**Cr$_5$Cu**} ring bridged by the second Cu^{II} centre, which may inspire future investigations on the stability of different bridging situations in polymetallic rings.

No ammonium cation is present in the dominant {**Cr$_5$Cu$_2$**} or {**Cr$_6$Cu**} ring products, which suggests that these are formed from the part of the hourglass where the ammonium cations and Piv$^-$ are lost in the primary fragmentation step. This is possibly due to insufficient space in the central cavity of a closed seven-metal species to bind an ammonium cation. Instead, Na^+ was found in the heptametallic species observed, where it is likely located in the centre of the ring as the DFT optimised structures suggest (Figures S11, S13). We have previously found that Na^+ is too small for a good fit for the cavity of an octametallic ring, both in the bulk and the gas phase,[28,53] and might hence be better suited for heptametallic species. The formation of {**Cr$_5$Cu$_2$**} from {**Cr$_{10}$Cu$_2$**}, likely occurring in a concerted step, implies that {**Cr$_5$**} is also formed. As discussed above, we have a low number of {**Cr$_5$**} ions (Figure 2a top), which is likely due to the relatively higher stability of heptametallic rings and the preference of the charge-carrier Na^+ to remain with {**Cr$_5$Cu$_2$**}, which complicates the detection of {**Cr$_5$**} cations. Our data suggests that {**Cr$_5$**} can occur in different conformations and/or topologies, potentially either as chains and/or rings (Supplementary Dataset).

The mechanism associated with smaller mass losses shows the stepwise disruption of the hourglasses, starting with the loss of one **Cu^{II}** centre along with two ligands. The formed {**Cr$_{10}$Cu**} and {**Cr$_{12}$Cu**} products are likely also closed due to their narrow and unimodal CCS_{N2} distributions (Figure 3, Table 1), and require the formation of new bonds on the experimental timescale. The {**Cr$_{12}$Cu**} distribution is significantly wider than for {**Cr$_{10}$Cu**}, indicating a higher conformational flexibility. The same qualitative trend was observed in the next fragmentation step, where the second ammonium cation is lost, predominantly along with a pivalate. After that, the second **Cu^{II}** centre dissociates along with two anionic ligands, leading to ions of the type {**Cr$_{10}$**} and {**Cr$_{12}$**}. Here both ions exhibit narrow CCS_{N2} distributions, once more suggesting cyclic structures.

*Disassembly of {**Cr$_{12}$Gd$_4$**}.* If similar disassembly mechanisms take place for [{**Cr$_{12}$Gd$_4$**} – Piv]$^+$ as for the hourglass ions, we would also expect smaller closed structures, of the type {**Cr$_6$Gd**} (as discussed above and in Table S1) or {**Cr$_6$Gd$_2$**}. For the second route involving low mass loss, we would expect the stepwise disruption of the {**Cr$_6$**} chains, again followed by

rearrangements to closed structures, as the {**Cr$_6$**} chains are more accessible for gas collisions and less strongly bound than the {**Gd$_4$**} unit.

The fragmentation of the ion [{**Cr$_{12}$Gd$_4$**} – Piv]$^+$ follows similar routes as [{**Cr$_x$Cu$_2$**} + Na]$^+$ (x = 10, 12) and confirms our hypothesis that the mechanisms observed for the hourglass ions can be transferred to other polymetallic complexes. Here, after the loss of one secondary ammonium cation along with a fluoride, the disassembly associated with higher mass loss leads to {**Cr$_6$Gd$_2$**} and subsequently to {**Cr$_5$Gd$_2$**} complexes, for which the comparisons with previously reported CCS_{N2} values clearly indicate closed structures.

The second disassembly mechanism of the {**Cr$_{12}$Gd$_4$**} cluster shows the loss of the second [$NH_2{}^nPr_2$]$^+$ and a pivalate, followed by multiple dissociation steps in which {**Cr**Piv$_3$} is lost. Here the loss of five {**Cr**Piv$_3$} units, occurring as the most abundant pathways, exceeds the number of pivalates present in a {**Cr$_6$**} chain and suggests either major rearrangements, or the disruption of the second {**Cr$_6$**} unit before the complete dissociation of the first. The CCS_{N2} distributions of the occurring products indicate more flexible structures (larger peak widths) than the precursor [{**Cr$_{12}$Gd$_4$**} – Piv]$^+$, however most of the products still appear with unimodal conformations (similarly to the fragments of [{**Cr$_{12}$Cu$_2$**} + Na]$^+$). This suggests that no major ring perturbation takes place and both horseshoe units are possibly disrupted simultaneously. In either case, the {**Cr**Piv$_3$} leaving group seems to be the driving force of this disassembly route, similar to previous observations.[25,28]

Conclusions

For the three studied compounds {**Cr$_x$Cu$_2$**} (x = 10, 12) and {**Cr$_{12}$Gd$_4$**}, the formation of smaller rings *via* rearrangements and newly established connectivities suggests a “self-healing” capability upon collision-induced dissociation, driven by the stability of closed, polymetallic species. Several of the latter were formed including {**Cr$_6$Cu**}, {**Cr$_5$Cu$_2$**}, {**Cr$_5$Cu**}, {**Cr$_{10}$Cu**}, {**Cr$_{10}$**}, {**Cr$_{12}$Cu**}, {**Cr$_{12}$**}, {**Cr$_6$Gd$_2$**} and {**Cr$_5$Gd$_2$**}, which we identified by ion mobility. This workflow can potentially inspire new applications in materials science, if these or similar complexes can be made in isolable quantities, and in general aid the design process of polymetallic complexes by identifying feasible targets. We also propose a simple method to assign whether a polymetallic complex exists as a closed or open structure, and this approach can in the future be adapted for other compound families. This workflow, with some modifications, has great

promise for the structural characterisation of larger metallosupramolecular compounds, and so has the diagnostic use of the tandem mass spectra to predict the precursor structure. As reliable computations and X-Ray crystallography are often not feasible, IM-MS is an important expansion of the available analytical methods for these systems.[54]

References

1. Dixit, S. M., Polasky, D. A. & Ruotolo, B. T. Collision induced unfolding of isolated proteins in the gas phase: past, present, and future. *Curr. Opin. Chem. Biol.* **42**, 93–100 (2018).

2. Hall, Z., Politis, A. & Robinson, C. V. Structural modeling of heteromeric protein complexes from disassembly pathways and ion mobility-mass spectrometry. *Structure* **20**, 1596–1609 (2012).

3. Zhou, M. & Wysocki, V. H. Surface Induced Dissociation: Dissecting Noncovalent Protein Complexes in the Gas phase. *Acc. Chem. Res.* **47**, 1010–1018 (2014).

4. Vallejo, D. D. *et al.* Mass Spectrometry Methods for Measuring Protein Stability. *Chem. Rev.* **122**, 7690–7719 (2022).

5. Christofi, E. & Barran, P. Ion Mobility Mass Spectrometry (IM-MS) for Structural Biology: Insights Gained by Measuring Mass, Charge, and Collision Cross Section. *Chem. Rev.* **123**, 2902–2949 (2023).

6. Troiani, F. *et al.* Molecular engineering of antiferromagnetic rings for quantum computation. *Phys. Rev. Lett.* **94**, 1–4 (2005).

7. Timco, G. A. *et al.* Engineering the coupling between molecular spin qubits by coordination chemistry. *Nat. Nanotechnol.* **4**, 173–178 (2009).

8. Fernandez, A. *et al.* Making hybrid [n]-rotaxanes as supramolecular arrays of molecular electron spin qubits. *Nat. Commun.* **7**, 1–6 (2016).

9. Lockyer, S. J. *et al.* Five-Spin Supramolecule for Simulating Quantum Decoherence of Bell States. *J. Am. Chem. Soc.* **144**, 16086–16092 (2022).

10. Lewis, S. M. *et al.* Use of Supramolecular Assemblies as Lithographic Resists. *Angew. Chem., Int. Ed.* **56**, 6749–6752 (2017).

11. Lewis, S. M. *et al.* Plasma-Etched Pattern Transfer of Sub-10 nm Structures Using a Metal-Organic Resist and Helium Ion Beam Lithography. *Nano Lett.* **19**, 6043–6048 (2019).

12. Lewis, S. M. *et al.* Tuning the Performance of Negative Tone Electron Beam Resists for the Next Generation Lithography. *Adv. Funct. Mater.* **2202710**, (2022).

13. Wang, H., Li, Y., Li, N., Filosa, A. & Li, X. Increasing the size and complexity of discrete 2D metallosupramolecules. *Nat. Rev. Mater.* **6**, 145–167 (2021).

14. McTernan, C. T., Davies, J. A. & Nitschke, J. R. Beyond Platonic: How to Build Metal-Organic Polyhedra Capable of Binding Low-Symmetry, Information-Rich Molecular Cargoes. *Chem. Rev.* **122**, 10393–10437 (2022).

15. Saha, R., Mondal, B. & Mukherjee, P. S. Molecular Cavity for Catalysis and Formation of Metal Nanoparticles for Use in Catalysis. *Chem. Rev.* **122**, 12244–12307 (2022).

16. Kroto, H. W., Heath, J. R., O'Brien, S. C., Curl, F. W. & Smalley, R. E. C60: Buckminsterfullerene. *Nature* **318**, 162–163 (1985).

17. Curl, R. F. Dawn of the Fullerenes: Experiment and Conjecture. *Nobel Lecture* (1996).

18. Kroto, H. W. Symmetry, Space, Stars, and C60. *Nobel Lecture* (1996).

19. Smalley, R. E. Discovering the Fullerenes. *Nobel Lecture* (1996).

20. Miras, H. N. *et al.* Solution identification and solid state characterisation of a heterometallic polyoxometalate {Mo11V7}: [Mo VI11VV5VIV2O52(μ9-SO3)]7-. *Chem. Commun.* **52**, 4703–4705 (2008).

21. Wilson, E. F. *et al.* Probing the self-assembly of inorganic cluster architectures in solution with cryospray mass spectrometry: Growth of polyoxomolybdate clusters and polymers mediated by silver(I) ions. *J. Am. Chem. Soc.* **130**, 13876–13884 (2008).

22. Yan, J., Long, D. L., Wilson, E. F. & Cronin, L. Discovery of heteroatom-"embedded" TeC(W18O 54) nanofunctional polyoxometalates by use of cryospray mass spectrometry. *Angew. Chem., Int. Ed.* **48**, 4376–4380 (2009).

23. Nadal, L. V. *et al.* Nucleation mechanisms of molecular oxides: A study of the assembly-dissassembly of [W6O19]2- by theory and mass spectrometry. *Angew.*

Chem., Int. Ed. **48**, 5452–5456 (2009).

24. Miras, H. N., Wilson, E. F. & Cronin, L. Unravelling the complexities of inorganic and supramolecular self-assembly in solution with electrospray and cryospray mass spectrometry. *Chem. Commun.* 1297–1311 (2009) doi:10.1039/b819534j.

25. Geue, N. *et al.* Disassembly Mechanisms and Energetics of Polymetallic Rings and Rotaxanes. *J. Am. Chem. Soc.* **144**, 22528–22539 (2022).

26. Engelhardt, L. P. *et al.* Octa-, deca-, trideca-, and tetradecanuclear heterometallic cyclic chromium-copper cages. *Angew. Chem., Int. Ed.* **47**, 924–927 (2008).

27. Larsen, F. K. *et al.* Horseshoes, Rings, and Distorted Rings: Studies of Cyclic Chromium-Fluoride Cages. *Angew. Chem., Int. Ed.* **42**, 5978–5981 (2003).

28. Geue, N. *et al.* Adduct Ions as Diagnostic Probes for Metallosupramolecular Complexes using Ion Mobility Mass Spectrometry. *Inorg. Chem.* **62**, 2672–2679 (2023).

29. McRobbie, A. *et al.* Chromium chains as polydentate fluoride ligands for lanthanides. *Chem. Commun.* **47**, 6251–6253 (2011).

30. Shrivastav, V., Nahin, M., Hogan, C. J. & Larriba-Andaluz, C. Benchmark Comparison for a Multi-Processing Ion Mobility Calculator in the Free Molecular Regime. *J. Am. Soc. Mass Spectrom.* **28**, 1540–1551 (2017).

31. Echt, O., Kreisle, D., Knapp, M. & Recnagel, E. Evolution of 'magic numbers' in mass spectra of water clusters. *Chem. Phys. Lett.* **108**, 401–407 (1984).

32. Sakurai, M., Watanabe, K., Sumiyama, K. & Suzuki, K. Magic numbers in transition metal (Fe, Ti, Zr, Nb, and Ta) clusters observed by time-of-flight mass spectrometry. *J. Chem. Phys.* **111**, 235–238 (1999).

33. Tsunoyama, H. & Tsukuda, T. Magic numbers of gold clusters stabilized by PVP. *J. Am. Chem. Soc.* **131**, 18216–18217 (2009).

34. Cole, H. L., Kalapothakis, J. M. D., Bennett, G., Barran, P. E. & MacPhee, C. E. Characterizing early aggregates formed by an amyloidogenic peptide by mass spectrometry. *Angew. Chem., Int. Ed.* **49**, 9448–9451 (2010).

35. Ohshimo, K., Takahashi, T., Moriyama, R. & Misaizu, F. Compact non-rock-salt

structures in sodium fluoride cluster ions at specific sizes revealed by ion mobility mass spectrometry. *J. Phys. Chem. A* **118**, 9970–9975 (2014).

36. McInnes, E. J. L., Timco, G. A., Whitehead, G. F. S. & Winpenny, R. E. P. Heterometallic Rings: Their Physics and use as Supramolecular Building Blocks. *Angew. Chem., Int. Ed.* **54**, 14244–14269 (2015).

37. Hoshino, N., Nakano, M., Nojiri, H., Wernsdorfer, W. & Oshio, H. Templating odd numbered magnetic rings: Oxovanadium heptagons sandwiched by β-cyclodextrins. *J. Am. Chem. Soc.* **131**, 15100–15101 (2009).

38. Tian, H., Bao, S. S. & Zheng, L. M. Cyclic single-molecule magnets: From the odd-numbered heptanuclear to a dimer of heptanuclear dysprosium clusters. *Chem. Commun.* **52**, 2314–2317 (2016).

39. McInnes, E. J. L. *et al.* Solvothermal synthesis of [Cr10(μ-O2CMe)10(μ-OR)20] 'chromic wheels' with antiferromagnetic (R = Et) and ferromagnetic (R = Me) (Cr(III)···Cr(III). *Chem. Commun.* **10**, 89–90 (2001).

40. Low, D. M. *et al.* A family of ferro- And antiferromagnetically coupled decametallic chromium(m) wheels. *Chem. Eur. J.* **12**, 1385–1396 (2006).

41. Sun, L., Zhang, J. & Cui, S. Solvothermal synthesis, structure, and magnetic property for nano-'chromic wheels' [Cr10(μ-O2CMe)10(μ-OMe)10(μ-OEt)10]. *Polyhedron* **26**, 2169–2173 (2007).

42. Gologan, B., Green, J. R., Alvarez, J., Laskin, J. & Cooks, R. G. Ion/surface reactions and ion soft-landing. *Phys. Chem. Chem. Phys.* **7**, 1490–1500 (2005).

43. Verbeck, G., Hoffmann, W. & Walton, B. Soft-landing preparative mass spectrometry. *Analyst* **137**, 4393–4407 (2012).

44. Laskin, J., Johnson, G. E., Warneke, J. & Prabhakaran, V. From Isolated Ions to Multilayer Functional Materials Using Ion Soft Landing. *Angew. Chem., Int. Ed.* **57**, 16270–16284 (2018).

45. Fremdling, P. *et al.* A Preparative Mass Spectrometer to Deposit Intact Large Native Protein Complexes. *ACS Nano* (2022) doi:10.1021/acsnano.2c04831.

564 46. Esser, T. K. *et al.* Mass-selective and ice-free electron cryomicroscopy protein sample
565 preparation via native electrospray ion-beam deposition. *PNAS Nexus* **1**, 1–13 (2022).

566 47. Johnson, G. E., Gunaratne, K. D. D. & Laskin, J. In situ SIMS and IR spectroscopy of
567 well-defined surfaces prepared by soft landing of mass-selected ions. *J. Vis. Exp.* 1–13
568 (2014) doi:10.3791/51344.

569 48. Su, P. *et al.* Design and Performance of a Dual-Polarity Instrument for Ion Soft
570 Landing. *Anal. Chem.* **91**, 5904–5912 (2019).

571 49. Samayoa-Oviedo, H. Y. *et al.* Design and Performance of a Soft-Landing Instrument for
572 Fragment Ion Deposition. *Anal. Chem.* **93**, 14489–14496 (2021).

573 50. Faull, P. A. *et al.* Gas-phase metalloprotein complexes interrogated by ion mobility-
574 mass spectrometry. *Int. J. Mass Spectrom.* **283**, 140–148 (2009).

575 51. Bleiholder, C., Dupuis, N. F., Wyttenbach, T. & Bowers, M. T. Ion mobility-mass
576 spectrometry reveals a conformational conversion from random assembly to β-sheet
577 in amyloid fibril formation. *Nat. Chem.* **3**, 172–177 (2011).

578 52. Beveridge, R. *et al.* A Mass-Spectrometry-Based Framework To Define the Extent of
579 Disorder in Proteins. *Anal. Chem.* (2014) doi:10.1016/b978-0-12-809633-8.20271-9.

580 53. Sañudo, E. C. *et al.* Proton NMR Study of Cr - Co Heterometallic Wheel Complexes.
581 *Inorg. Chem.* **48**, 9811–9818 (2009).

582 54. Geue, N., Winpenny, R. E. P. & Barran, P. E. Structural characterisation methods for
583 supramolecular chemistry that go beyond crystallography. *Chem. Soc. Rev.* **51**, 8–27
584 (2022).

585 55. Ochsenbein, S. T. *et al.* Studies of finite molecular chains: Synthesis, structural,
586 magnetic and inelastic neutron scattering studies of hexa- And heptanuclear
587 chromium horseshoes. *Chem. Eur. J.* **14**, 5144–5158 (2008).

588 56. Fort, K. L. *et al.* Expanding the structural analysis capabilities on an Orbitrap-based
589 mass spectrometer for large macromolecular complexes. *Analyst* **143**, 100–105
590 (2018).

591 57. Giles, K. *et al.* A Cyclic Ion Mobility-Mass Spectrometry System. *Anal. Chem.* **91**, 8564–

8573 (2019).

58. Kertesz, T. M., Hall, L. H., Hill, D. W. & Grant, D. F. CE50: Quantifying Collision Induced Dissociation Energy for Small Molecule Characterization and Identification. *J. Am. Soc. Mass Spectrom.* **20**, 1759–1767 (2009).

59. Hill, D. W. *et al.* Correlation of Ecom 50 values between mass spectrometers: Effect of collision cell radiofrequency voltage on calculated survival yield. *Rapid Commun. Mass Spectrom.* **26**, 2303–2310 (2012).

60. Chakraborty, P. *et al.* Dissociation of Gas Phase Ions of Atomically Precise Silver Clusters Reflects Their Solution Phase Stability. *J. Phys. Chem. C* **121**, 10971–10981 (2017).

61. Ruotolo, B. T., Benesch, J. L. P., Sandercock, A. M., Hyung, S. J. & Robinson, C. V. Ion mobility-mass spectrometry analysis of large protein complexes. *Nat. Protoc.* **3**, 1139–1152 (2008).

62. Stow, S. M. *et al.* An Interlaboratory Evaluation of Drift Tube Ion Mobility-Mass Spectrometry Collision Cross Section Measurements. *Anal. Chem.* **89**, 9048–9055 (2017).

63. Dolg, M., Stoll, H. & Preuss, H. A combination of quasirelativistic pseudopotential and ligand field calculations for lanthanoid compounds. *Theor. Chim. Acta* **85**, 441–450 (1993).

64. Dolg, M., Stoll, H., Savin, A. & Preuss, H. Energy-adjusted pseudopotentials for the rare earth elements. *Theor. Chim. Acta* **75**, 173–194 (1989).

65. Rigaku Corporation. CrysAlisPro Software System, Version 1.171.42.xx. (2022).

66. Sheldrick, G. M. SHELXT - Integrated space-group and crystal-structure determination. *Acta Crystallogr. Sect. A Found. Crystallogr.* **71**, 3–8 (2015).

67. Sheldrick, G. M. Crystal structure refinement with SHELXL. *Acta Crystallogr. Sect. C Struct. Chem.* **71**, 3–8 (2015).

68. Dolomanov, O. V., Bourhis, L. J., Gildea, R. J., Howard, J. A. K. & Puschmann, H. OLEX2: A complete structure solution, refinement and analysis program. *J. Appl. Crystallogr.*

620 **42**, 339–341 (2009).

621 ## Methods

622 *Synthesis*. {**$Cr_{12}Cu_2$**} was synthesised according to our previous work.[26] {**$Cr_{10}Cu_2$**} was made
623 similarly to $[NH_2Et_2]_2[\mathbf{Cr_{10}Cu_2}F_{14}(O_2C^tBu)_{22}]$,[27] but the precursor diethylamine was replaced
624 with dipropylamine. Elemental analysis (%) calcd. for {**$Cr_{10}Cu_2$**}: C 43.84, H 6.94, N 0.84,
625 Cr 15.56, Cu 3.80; found: C 44.13, H 6.99, N 0.89, Cr 15.42, Cu 3.86. {**$Cr_{12}Gd_4$**} was synthesized
626 similarly to $[NH_2Et_2]_2[\mathbf{Cr_{12}Gd_4}F_{21}(O_2C^tBu)_{29}]$,[29] by using the previously reported[55]
627 $[(NH_2{}^nPr_2)_3\mathbf{Cr_6}F_{11}Piv_{10}]_2$ as the reactant instead of $[(NH_2Et_2)_3\mathbf{Cr_6}F_{11}Piv_{10}]_2$. Elemental analysis
628 (%) calcd. for {**$Cr_{12}Gd_4$**}: C 39.38, H 6.17, N 0.58, Cr 13.03, Gd 13.13; found: C 39.54, H 6.21,
629 N 0.63, Cr 12.85, Gd 13.45. All reagents and solvents were purchased from Alfa, Fisher
630 Scientific, Fluorochem or Sigma-Aldrich and used without further purification.

631 *Sample Preparation.* Samples were prepared in 4:1 toluene/methanol with 500 μM NaI.
632 Analyte concentrations of 200 – 500 μM were typically used for IM-MS and MS measurements.

633 *nano-Electrospray Ionisation (nESI).* Samples were ionised and transferred to the gas phase
634 with a nESI source and were sprayed from borosilicate glass capillaries (World Precision
635 Instruments, Stevenage, UK). The latter were pulled on the Flaming/Brown P-2000 laser puller
636 (Sutter Instrument Company, Novato, CA, US). The capillary voltage (typically 1.0 - 1.8 kV) was
637 applied through a platinum wire (Diameter 0.125 mm, Goodfellow, Huntingdon, UK) inserted
638 into the nESI capillaries. Source temperatures of 23 °C (Cyclic) or 30 °C (Q Exactive UHMR)
639 were applied.

640 *Tandem Mass Spectrometry (MS^2).* The Q Exactive Ultra-High-Mass-Range (UHMR) Hybrid
641 Quadrupole-Orbitrap Mass Spectrometer (Thermo Fisher) was used for the derivation of the
642 E_{50} values *via* MS^2 experiments, and more precisely collision-induced dissociation (CID).[56]
643 Target ions were *m/z*-isolated in a quadrupole filter, accelerated to a user-defined kinetic
644 energy (E_{lab}: 0 - 300 eV) and injected into the higher-energy C-trap dissociation (HCD) cell,
645 which contained nitrogen gas (trapping gas pressure parameter: 2.0). Non-fragmented
646 precursor ions and fragment ions were transferred to the Orbitrap mass analyser (AGC target:
647 3E6 ions, maximum inject time: 100 ms, resolution: 25000).

648 *Ion mobility mass spectrometry (IM-MS)* experiments were performed on a Select Series Cyclic
649 IMS (Waters).[57] Following ionization (Cone Voltage: 20 - 60 V, Source Offset: 10 - 20 V, Purge

Gas: 0 – 300 L/h), ions were transferred to the trap and activated *via* collisions with nitrogen gas, if appropriate (Trap Voltage: 0 – 200 V, Gas Flow: 5 mL/min). Ions are further injected to the cyclic ion mobility drift ring (Stepwave Ion Guide RF: 300 – 700 V) and separated by using a non-uniform electric field under a constant nitrogen pressure with travelling waves (TW, Height: 20 - 22 V, Velocity: 375 m/s, Gas Flow: 40 mL/min), pushing the ions through the drift ring. Ions travelled one pass in the cyclic drift ring ("single path", separation time: 2 – 60 ms) and were then transferred (Transfer Voltage: 4 – 15 V) to a time-of-flight mass analyser.

Data Processing. E_{50} values were obtained a method described in our previous works.[25,28] Mass spectra were recorded at different collision energies and the share of the precursor ion count, relative to the total ion count ("survival yield"), was plotted vs. the collisional energy in the centre-of-mass frame (E_{com}, Figures S3, S9). Survival yield plots were fitted with a sigmoidal Hill function (Hill1 function in OriginPro 2020b), yielding the point (E_{50}) at which the survival yield reaches 0.5 or 50%. This E_{50} value is known as a relative measure of precursor ion stability.[58–60]

Experimentally obtained arrival time distributions (ATD) were converted to collisional cross section distributions ${}^{TW}CCS_{N2}$ (TW: ‚Travelling Waves') *via* published calibration procedures.[61] The Agilent tune mix was used as a calibrant.[62]

Density Functional Theory and Collision Cross Section Calculations. Analogous to our previous works,[25,28] density functional calculations were carried out using the same effective core potentials and basis sets for Cu, Cr, C, N, O, F and H, assuming high spin ferromagnetically coupled metals. For $\mathbf{Gd^{III}}$, it was necessary to use an alternative effective core potential, including 7f electrons in core,[63] with the corresponding (7s6p5d)/(5s4p3d) contracted valence basis set.[64]

Theoretical collision cross section values (${}^{TH}CCS_{N2}$, TH: ‚Theoretical') were obtained from the software IMoS by using the trajectory method in nitrogen gas including quadrupole potential (number of orientations: 3, gas molecules per orientation: 300,000, temperature: 298 K, pressure: 101,325 Pa = 1 atm).[30]

Crystallographic Data. Single crystals of {$\mathbf{Cr_{10}Cu_2}$} and {$\mathbf{Cr_{12}Gd_4}$} were grown by slow diffusion of acetonitrile into toluene solutions of the respective complexes. ORTEP Structures of {$\mathbf{Cr_{10}Cu_2}$} (Figure S16) and {$\mathbf{Cr_{12}Gd_4}$} (Figure S17) can be found in the Supporting Information

along with crystallographic refinement details (Table S3). Crystal structures are also presented in Figure 1a and 1c as well as in the Supplementary Dataset, respectively.

X-ray diffraction data were collected using a dual wavelength Rigaku FR-X rotating anode diffractometer using MoKα (λ = 0.71073 Å) radiation, equipped with an AFC-11 4-circle goniometer, VariMAX^{TM} microfocus optics, a Hypix-6000HE detector and an Oxford Cryosystems 800 plus nitrogen flow gas system, at a temperature of 100K. Data were collected and reduced using Rigaku CrysAlisPro v42[65] and absorption correction was performed using empirical methods (SCALE3 ABSPACK) based upon symmetry-equivalent reflections combined with measurements at different azimuthal angles. The phase problem was solved using SHELXT and the structural model refined against all F^2 values using SHELXL,[66,67] implemented through Olex2 v1.5.[68] All non-solvent atoms were refined anisotropically. Hydrogen atoms were placed in calculated positions and refined using idealised geometries and assigned fixed isotropic displacement parameters.

Acknowledgements

N. G. is grateful for funding through the President's Doctoral Scholar Award by The University of Manchester. We acknowledge the support of EPSRC through the strategic equipment award EP/T019328/1, the European Research Council for funding the MS SPIDOC H2020-FETOPEN-1-2016-2017-801406 and Waters Corporation, particularly Dr. Dale Cooper-Shepherd, for their continued support of mass spectrometry research within the Michael Barber Centre for Collaborative Mass Spectrometry. R. E. P. W. thanks the EPSRC for an Established Career Fellowship (EP/R011079/1) and the European Research Council for an Advanced Grant (ERC-2017-ADG-786734). The authors also thank Aidan Rawlinson, for support with data analysis software, Tom S. Bennett, The University of Manchester, for support with the design of figures, EPSRC for funding an X-ray diffractometer (EP/K039547/1) as well as the staff in the MS and Separation Science, and the XRD Facilities in the Faculty of Science and Engineering, The University of Manchester for their assistance. The authors would also like to acknowledge the assistance given by Research IT and the use of the Computational Shared Facility at The University of Manchester.

Conflict of Interests

There are no conflicts to declare.

Author Contributions

N.G., R.E.P.W and P.E.B conceived of the idea for this study. N.G. performed the mass spectrometry and ion mobility mass spectrometry experiments as well as the data analysis and theoretical CCS_{N2} calculations. G.A.T. synthesised the polymetallic complexes and collected their crystal structures. G.F.S.W. refined the crystal structures. N.A.B. performed the DFT calculations. N.G. wrote the manuscript with input from R.E.P.W, P.E.B. and all the other authors.

Data Availability Statement

The supporting data referred to in this manuscript is contained within a supplementary information document and in a supplementary dataset available on Figshare https://figshare.com/articles/dataset/Geue_Supplementary_Dataset_Heterocluster_Paper_zip/21751442. The latter includes the raw data of all ion mobility mass spectrometry and mass spectrometry measurements as well as the DFT calculation outputs and crystal structures. CCDC 2226287−2226288 contain the supplementary crystallographic data of {$\mathbf{Cr_{10}Cu_2}$} and {$\mathbf{Cr_{12}Gd_4}$}. These data can be obtained free of charge via www.ccdc.cam.ac.uk/data_request/cif, or by emailing data_request@ccdc.cam.ac.uk, or by contacting The Cambridge Crystallographic Data Centre, 12 Union Road, Cambridge CB2 1EZ, UK; fax: +44 1223 336033.